Electronic and mechanical properties of few-layer borophene

Hongxia Zhong, Kaixiang Huang, Guodong Yu, and Shengjun Yuan[*]

School of Physics and Technology, Wuhan University, Wuhan 430072, People's Republic of China

We report first-principles calculations of electronic and mechanical properties of few-layer borophene with the inclusion of interlayer van der Waals (vdW) interaction. The anisotropic metallic behaviors are preserved from monolayer to few-layer structures. The energy splitting of bilayer borophene at Γ point near the Fermi level is about 1.7 eV, much larger than the values (0.5–1 eV) of other layered semiconductors, indicating much stronger vdW interactions in metallic layered borophene. In particular, the critical strains are enhanced by increasing the number of layers, leading to much more flexibility than that of monolayer structure. On the one hand, because of the buckled atomic structures, the out-of-plane negative Poisson's ratios are preserved as the layer number increases. On the other hand, we find that the in-plane negative Poisson's ratios disappear in layered borophene, which is very different from puckered black phosphorus. The negative Poisson's ratio will recover if we enlarge the interlayer distance to 6.3 Å. The physical origin behind the change of Poisson's ratios is the strong interlayer vdW interaction in layered borophene.

I. INTRODUCTION

Boron, next to carbon in the periodic table, has more than 16 bulk and numerous low-dimensional allotropes [1,2]. The polymorphism is originated from the electron deficiency, resulting in the multicenter B–B bonds, which is much more complicated than that in carbon [2]. Among the polymorphic structures, two-dimensional (2D) boron materials (borophene) have attracted extensive theoretical interests because of their remarkable physical and chemical properties [3–6]. A class of borophene has therefore been designed [7]. However, there was no evidence that the 2D boron sheets could be fabricated experimentally until 2015 [8]. Mannix *et al.* first reported the synthesis of 2-*Pmmn* borophene in ultrahigh vacuum conditions on Ag (111) surfaces by physical vapor deposition in Ref. [8]. Scanning tunneling microscopy characterization of the one-atom-thick 2D sheets revealed a hexagonal arrangement of boron atoms with an extra atom in the middle. Later, Feng *et al.* have also grown two boron sheets, a β_{12} sheet and χ_3 sheet on Ag(111) surfaces, and the β_{12} phase is found to be with gapless Dirac cones [9–11]. These two phases are in triangular lattices but in flat geometry and with a periodic arrangement of atom vacancies [9,10]. The observed phase depends on the deposition rate and temperature in the experiment, confirming the predicted large polymorphism of borophene.

The successful fabrications of borophene have inspired much followup works, especially for the buckled 2-*Pmmn* structure. Owing to its anisotropic atomic structure, the buckled borophene shows highly anisotropic metallic properties, very different from the semimetallic graphene [12] and semiconducting transition-metal dichalcogenides (TMDCs) [8,13–21]. The predicted Fermi velocity of hydrogenated borophene $(3.5 \times 10^6$ m/s) is nearly four times higher than that of graphene $(8.2 \times 10^5$ m/s) [22–24]. The investigated optical spectra attest high optical transparency (up to 100% transmission) predicted up to roughly 3 eV, making borophene more transparent than graphene [13]. Borophene thus can be considered as a good candidate of transparent conductive 2D material for photovoltaics and touch screens, due to its robust metallicity, high Fermi velocity, and ultrahigh optical transparency. Furthermore, pristine borophene has been predicted to exhibit phonon-mediated superconductivity with critical temperature T_c in the range of 10–20 K [25,26]. For the mechanical properties, the buckled borophene shows considerable toughness, and it has been demonstrated that the in-plane Young's modulus along the armchair direction (398 GPa nm) [8] can rival that of graphene (340 GPa nm) [12]. Notably, monolayer borophene is calculated to exhibit negative in-plane and out-of-plane Poisson's ratios. The negative Poisson's ratios of monolayer borophene make it worth further exploitation in many applications, such as medicine [27], tougher composites [28], national security and defenses [29,30]. In the following, we focus solely on the buckled 2-*Pmmn* borophene, a promising 2D material which has fantasy physical properties.

Previous theoretical studies of 2-*Pmmn* borophene mainly focused on the physical properties of monolayer borophene [13–15]. A comprehensive study of the electronic and elastic properties of the few-layer borophene is still lacking. Moreover, the physical properties of layered 2D materials are highly dependent on their thickness, such as the band crossover in hexagonal TMDCs which is originated from the interlayer van der Waals (vdW) interaction and variations of screening [31–33]. Therefore, it is of both fundamental and practical interests to attain a better understanding of the interlayer vdW interactions among the layered borophene. We note that it is inclined to form 3D boron clusters instead of 2D layered borophene by depositing additional boron atoms on monolayer flat β_{12} sheet and χ_3 borophene supported by Ag(111)

*s.yuan@whu.edu.cn

surfaces in Ref. [9], as a result of the saturation of the Ag–B interfacial interactions. However, in the experiments there were occasionally small islands observed of second layer, although with different structures comparing to the first layer [9]. Moreover, recent molecular dynamics study about borophene on different metal templates [34] shows that Au surface is the most favorable for bilayer formation due to its lowest binding ability with the boron sheet among Cu, Ag, Au surfaces. We thus believe that few-layer buckled 2-*Pmmn* borophene can be fabricated with different experimental method or a proper choice of the substrate.

In this paper, we present a comprehensive theoretical study of the electronic and elastic properties of few-layer borophene, using a first-principles approach including the vdW interaction. We first give a brief description of the numerical methods, and then discuss the chemical bonding nature of borophene, the structure and electronic properties of layered structure with different types of interlayer stacking, and determine the preferable stacking mode which has the lowest total energy. We will then focus on the layered structure with this stacking mode, and investigate the electronic and mechanical properties of bilayer, trilayer, and four-layer borophene. The out-of-plane and in-plane Poisson's ratios will be studied in detail, by considering the influence of the interlayer vdW interaction. We will summarize our main findings in the Conclusion.

II. METHODS

Our calculations are performed using the projector augmented wave (PAW) method [35] implemented in the Vienna *ab initio* simulation package (VASP) code [36,37]. Perdew, Burke, and Ernzerhof (PBE) form of the generalized gradient approximation (GGA) exchange-correlation functional with van der Waals corrections (vdW-DFT) [38–40] and the PAW pseudopotentials [35] are adopted. The cutoff energy is set to 500 eV after convergence tests. A Γ-centered Monkhorst-Pack k-point [41,42] grid of $15\times13\times1$ for one borophene unit cell is chosen for relaxations and the grid of $25\times23\times1$ for property calculations. In our current calculations, the total energy is converged to less than 10^{-5} eV. The maximum force is less than 0.02 eV/Å during the optimization. A vacuum space between neighboring supercells is set to be more than 25 Å to avoid spurious interactions. The crystal orbital Hamilton population (COHP) curves are calculated using the LOBSTER software [43].

For 2D orthorhombic borophene, there are four nonzero elastic stiffness constants C_{11}, C_{22}, C_{66}, and C_{12}, and the stress-strain relationship is obtained from Hooke's law under plane-stress condition [44].

$$\begin{pmatrix} \sigma_{xx} \\ \sigma_{yy} \\ \sigma_{xy} \end{pmatrix} = \begin{pmatrix} C_{11} & C_{12} & 0 \\ C_{21} & C_{22} & 0 \\ 0 & 0 & C_{66} \end{pmatrix} \begin{pmatrix} \varepsilon_{xx} \\ \varepsilon_{yy} \\ 2\varepsilon_{xy} \end{pmatrix}, \quad (1)$$

where C_{ij} ($i, j = 1, 2, 6$) is the in-plane stiffness tensor and is equal to the second partial derivative of strain energy E_s as a function of strain $\boldsymbol{\varepsilon}$ in the range $-2\% < \boldsymbol{\varepsilon} < 2\%$ with an increment of 0.5%, based on the following formula [45]:

$$E_s = \tfrac{1}{2}C_{11}\varepsilon_{xx}^2 + \tfrac{1}{2}C_{22}\varepsilon_{yy}^2 + C_{12}\varepsilon_{xx}\varepsilon_{yy} + 2C_{66}\varepsilon_{xy}^2. \quad (2)$$

The engineering strain is defined as $\varepsilon = (L - L_0)/L_0$, where L and L_0 are the lattice constants of the strained and unstrained structures, respectively. The E_s curves are nonsymmetric in our calculations. There is a minor difference between the positive and negative curves. We therefore take the average value [8,46]. Here, we get the elastic constants C_{ij} using the VASPKIT code [47]. Then, the Young's modulus E and Poisson's ratio ν can be derived as [48]

$$E_x = \frac{C_{11}C_{22} - C_{12}C_{21}}{C_{22}}, \quad E_y = \frac{C_{11}C_{22} - C_{12}C_{21}}{C_{11}}, \quad (3)$$

$$\nu_{xy} = \frac{C_{21}}{C_{22}}, \quad \nu_{yx} = \frac{C_{12}}{C_{11}}. \quad (4)$$

In order to describe the change of buckling height with the strain applied along $\boldsymbol{x}$ or $\boldsymbol{y}$ direction, the out-of-plane Poisson's ratio is defined as

$$\nu_{zx} = -\frac{\varepsilon_{zz}}{\varepsilon_{xx}}, \quad \nu_{zy} = -\frac{\varepsilon_{zz}}{\varepsilon_{yy}}, \quad (5)$$

where ν_{zx} (ν_{zy}) is the out-of-plane Poisson's ratio along $\boldsymbol{z}$ axis when the stress is applied along $\boldsymbol{x}$ ($\boldsymbol{y}$) direction, $\boldsymbol{\varepsilon}_{zz} = (b - b_0)/b_0$ is the strain along $\boldsymbol{z}$ axis, b and b_0 are the buckling heights of strained and unstrained structures.

The phonon dispersion calculations are based on PHONOPY code [49]. A $8\times3\times1$ supercell with $13\times9\times1$ k mesh is used to ensure the convergence. The *ab initio* molecular dynamics (AIMD) simulations are performed to evaluate the thermal stabilities of unstrained bilayer borophene. All AIMD simulations are performed using a 8×5 (160 atoms in total) superlattice in the canonical (NVT) ensemble. The superlattices are annealed for 10 ps with a time step of 1 fs in the simulations [50].

III. STRUCTURAL AND ELECTRONIC PROPERTIES

A. Chemical bonding nature of borophene

The ball-stick structures of monolayer buckled borophene are presented in Fig. 1(a). Our benchmark calculations on monolayer borophene give lattice constants of $a = 1.613$ Å and $b = 2.880$ Å, in good agreement with previous values [13–15,26,51]. There is a buckling along $\boldsymbol{b}$ direction with height $\Delta = 0.941$ Å, while no corrugations are observed along $\boldsymbol{a}$ direction. To analyze the nature of the chemical bonding in borophene, Fig. 1(b) shows our bonding analysis based on $-$pCOHP. The Fermi level is dominated by B1–B2 interactions. The amount of occupied bonding B–B between B1–B2 atoms is larger than those between B1–B3 atoms. It means that the bonding interaction between B1–B2 atoms is much stronger than that between B1–B3 atoms. This is consistent with the shorter bond length of B1–B2 (1.613 Å), compared with that of B1–B3 (1.855 Å). A delocalization of electrons over B1 and B3 atoms is through the formation of multicenter bonds along the zigzag direction. Such kind of resonant bonding can also explain the slightly longer bond length compared to classical B–B single bond (1.686 Å) [52]. On the other hand, B1 and B2 atoms form strong σ bond along the armchair direction.
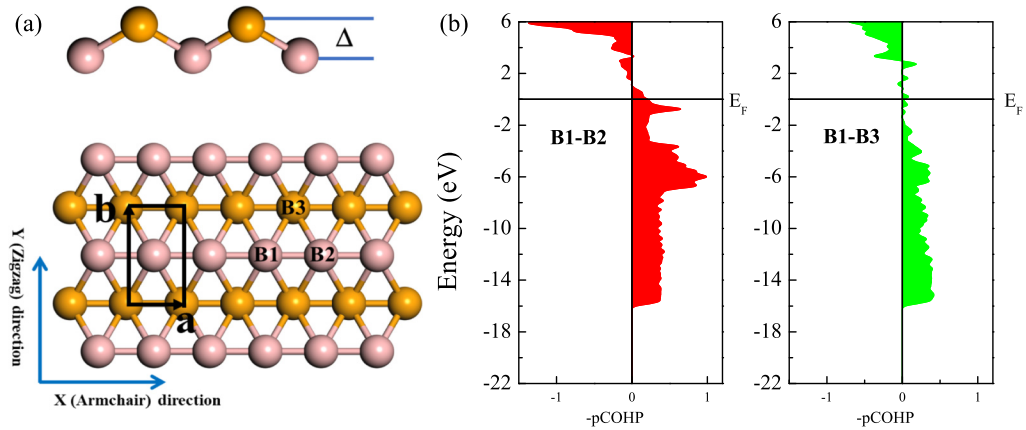
FIG. 1. (a) Side and top views of monolayer borophene. The atoms occupying the A and B sites are on different planes, separated by a distance $\Delta = 0.941$ Å. The blacked rectangle indicates a unit cell. The bond B1–B2 is along the armchair direction, and the bond B1–B3 is along the zigzag direction. (b) Negative projected COHP ($-$pCOHP) curves of monolayer borophene containing B1–B2 and B1–B3 interactions.

B. Geometry and stability of layered borophene

Since the structures of bilayer borophene are rather complicated, we only consider six stacking configurations (AA, AB, AAp, ABp, AAb, and ABb) with high symmetry in this work, as shown in Figs. 2(a)–2(c). There are three kinds of top views of these six stacking modes. For AA and AB stacking modes, the top layer is directly stacked on the bottom layer. The AAp (ABp) and AAb (ABb) stacking modes can be viewed as shifting half of the bond length along either B1–B2 or B1–B3 bond direction. Two kinds of side views, coming from the fact that the bottom layer could have the same buckling order as the top or the opposite, have been discussed. All sublayers are initially separated by a distance of 3.0 Å, and we use the optimized lattice constants of monolayer borophene as the initial lattice constants for bilayer structures. The in-plane lattice vectors and atomic positions are relaxed completely. We note that Gao *et al.* have discussed the bilayer configurations [53] of α phase, a theoretical predicted phase with holes doping

in hexagonal lattice. This work focuses solely on the buckled 2-*Pmmn* borophene, successfully fabricated on Ag(111) surface by physical vapor deposition [8].

The lattice parameters of the investigated structures are the same of $a = 1.610$ Å and $b = 2.898$ Å, with the same buckling height of 0.941 Å. The most notable difference among the six stacking modes is the interlayer distance between the top and bottom layers, varying from 3.072 Å in the AA stacking to 3.391 Å in the AB stacking. It can be seen that the energy of the system highly depends on its interlayer distance. To better understand this dependence and to ensure those stacks obtained from the free relaxions reach minimum energy of the system rather than a local minimum, we study the evolution of the total energy as a function of the interlayer distance for each system in Fig. 2(d). First, these six configurations have an energy minimum without phase transitions. Because different stacking order leads to different π-π interaction distance between delocalized states and thereby different interaction
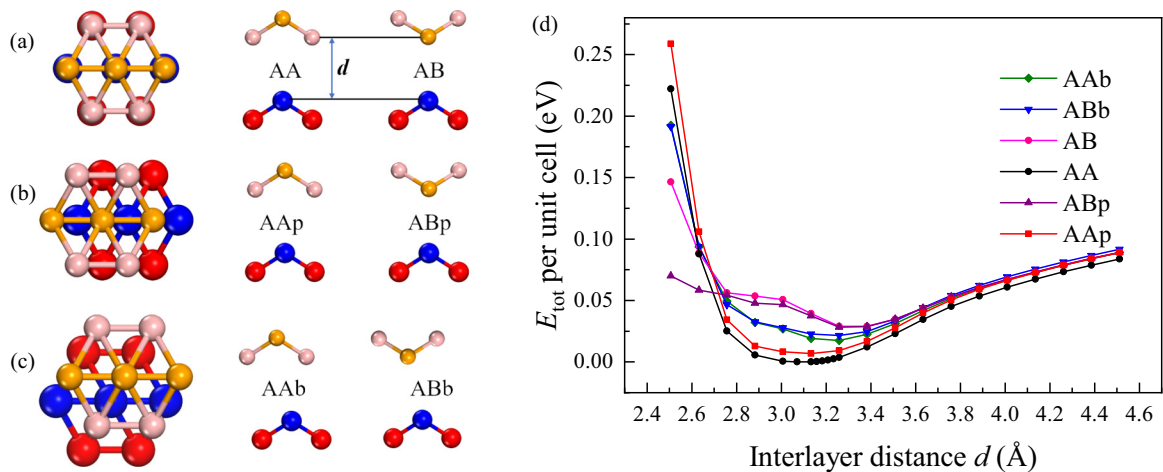
FIG. 2. Six high-symmetry configurations of bilayer borophene are (a) AA and AB with the same top view, (b) AAp and ABp, (c) AAb and ABb. (d) Total energy of these six considered stacking modes as a function of the interlayer distance between two nearest boron atoms of the top and bottom layers along z direction. The interlayer distance varies around the equilibrium distance of each configuration and all atoms are relaxed with this constraint. The lowest calculated total energy (in this case, the total energy associated with the AA configuration) was set to zero, and the others were calculated with respect to this one.
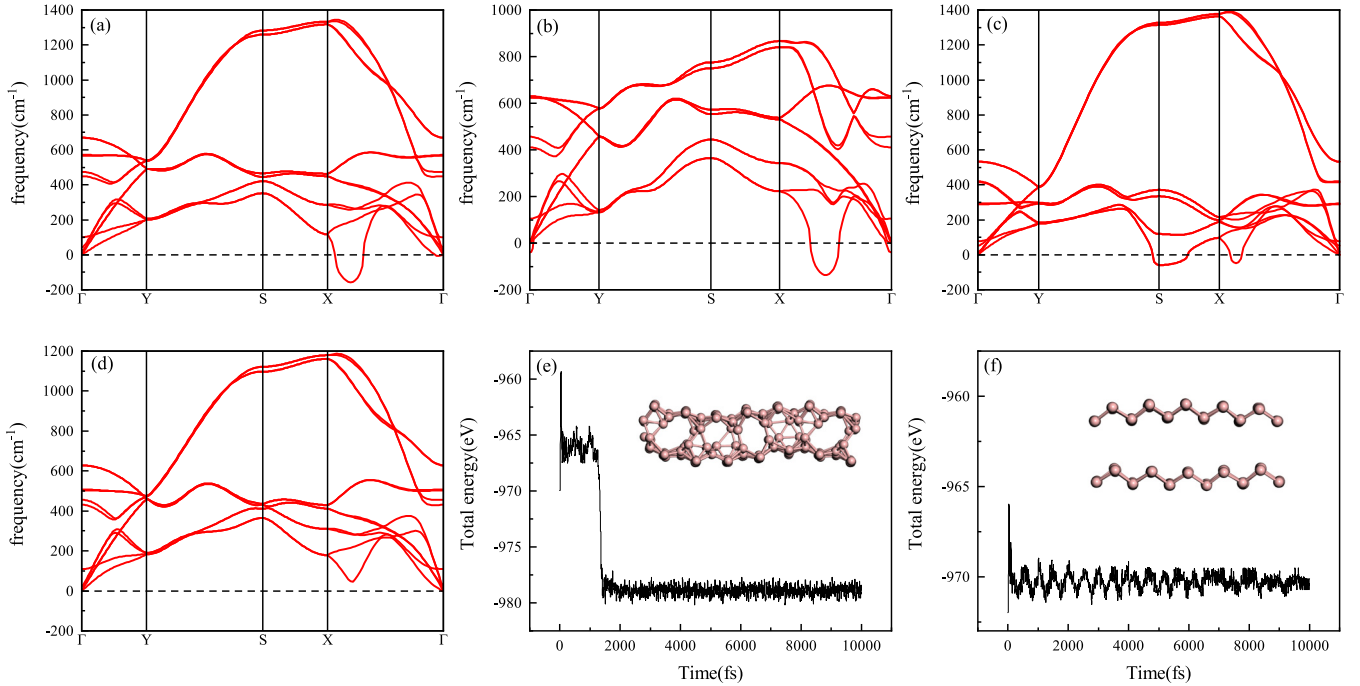
FIG. 3. Phonon dispersions of bilayer borophene at (a) free, (b) uniaxial tensile strain along armchair of 10%, (c) uniaxial tensile strain along zigzag of 10%, (d) biaxial tensile strain along armchair of 3%. Evolution of total energy versus simulation time in AIMD for unstrained bilayer borophene at (e) 300 K and (f) 200 K. The insets show the snapshots for the final equilibrium structures.

strength, the order of stability of the considered structures is as follows: AA > AAp > AAb > ABb > AB > ABp. AA stacking structure is found to be the most energetically preferred configuration with the smallest interlayer distance and corresponding strongest interlayer interaction. It is very different from other 2D materials whose preferred configurations are in AB stacking, such as graphene [54], silicene [55], black phosphorene [56], and hexagonal TMDCs [57,58]. Furthermore, the corresponding interlayer distance 3.072 Å is slightly smaller than the value (3.214 Å) of AB stacking phosphorene [56], which has also a buckled monolayer structure. It is worth to mention that the buckled AA stacking borophene studied in our paper has totally different atomic structure comparing to the flat alpha-phase borophene studied by Gao *et al.* in Ref. [53], in which the strong chemical bonding between the layers leads to much smaller interlayer distance (1.75 Å). Based on the AA stacking bilayer borophene, we take the stacking sequence of AAA and AAAA into trilayer and four-layer borophene structures, respectively.

To further examine the dynamical stability of strained layered borophene, we calculate the phonon dispersions of bilayer borophene shown in Fig. 3. The out-of-plane acoustic (ZA) branch has imaginary frequencies along Γ-X direction, indicating that the lattice exhibits instability against out-of-plane vibrations. For the uniaxial strain of 10% along armchair direction, the imaginary frequency of the ZA branch is still present in Γ-X direction. When the uniaxial strain is applied in zigzag direction, the imaginary frequency of the ZA branch in Γ-X direction decreases, but appears in S-X direction. Interestingly, such phonon mode remains stable under biaxial strain of 3% in Fig. 3(d). This stability is retained under larger biaxial strain. Since the phonon calculations does not take

temperature into account, we further do AIMD simulations to confirm the dynamical stability in Figs. 3(e) and 3(f). There is a phase transition for unstrained bilayer borophene at 300 K. The unstrained bilayer borophene loses long-range order, similar to the case of glass and liquid [59]. When the temperature decreases to be 200 K, the geometry of AA stacking bilayer borophene is well preserved. This indicates that although the AA stacking bilayer borophene is not stable at room temperature, it can be stable at low temperature or under biaxial strain.

C. Electronic properties of layered borophene

The electronic band structures of monolayer and AA stacking bilayer, trilayer, and four-layer borophene are shown in Fig. 4. Compared with the case of monolayer borophene [15], the Fermi level is crossed by more bands because of the band splitting. Hence, the robust metal feature is retained with the increasing of the layer number. The local band gaps resulting from the buckling at Γ and S points still exist. The band gap at Γ point decreases from 4.326 eV (monolayer) to 2.117 eV (four layer), as a result of the increasing band splitting with the increasing layer number. Because there is no splitting at S point, the band gap at this high-symmetry point barely depends on the layer number. Therefore, layered borophene behaves anisotropic in electronic properties resulting from the anisotropic atomic structure, and the electrical conductivity is expected to be confined along the uncorrugated armchair direction.

Compared to the band structure of monolayer borophene, the addition of layers results in the band splitting around the Γ point in the band structures of layered borophene. The values of
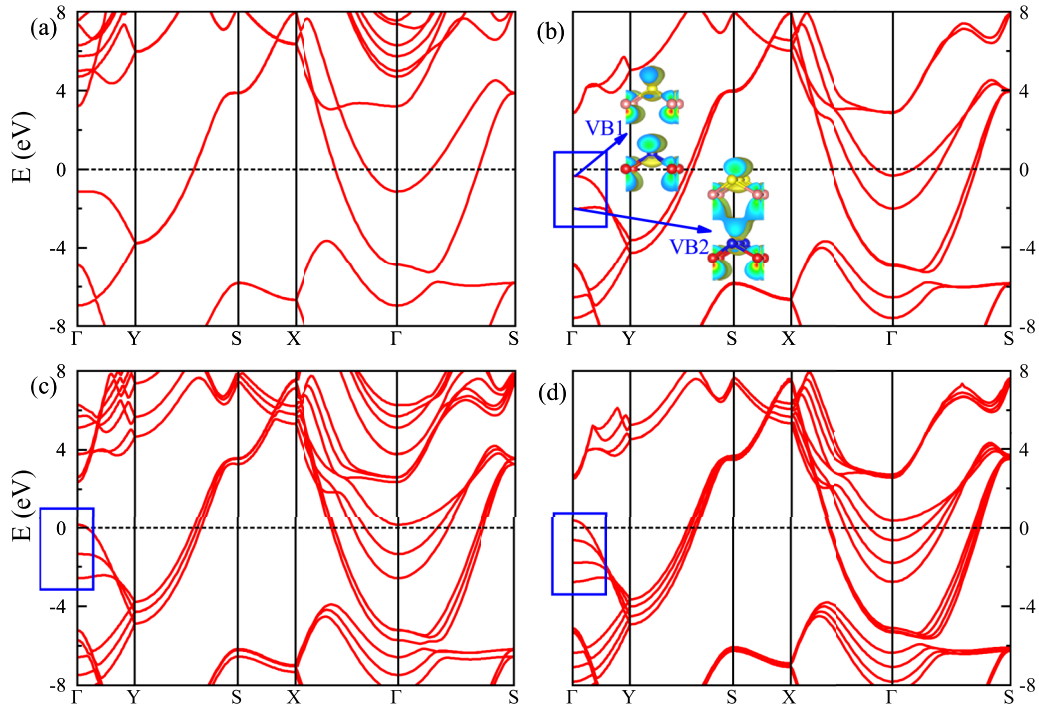
FIG. 4. (a)–(d) Band structures of monolayer, bilayer, trilayer, and four-layer borophene, respectively. The Fermi level is set to zero. Blue rectangles show the band splitting near the Fermi level. The insets of (b) show the isosurfaces of the charge density corresponding to VB1 and VB2, respectively.

band splitting at the Γ point for bilayer, trilayer, and four-layer borophene are 1.681, 1.358, and 1.039 eV, respectively. The value of bilayer borophene band splitting is much larger than that (0.5–1 eV) of bilayer MoS_2 [57] and black phosphorus [56]. This indicates that the interlayer interaction in metallic layered borophene is much stronger than those in other semi-conducting 2D materials. To understand the interlayer interaction contribution, we plot the isosurfaces of the charge density corresponding to the VB1 and VB2 of bilayer borophene as insets of Fig. 4(b), respectively. According to the spatial distri-bution of the charge density, we can recognize the antibonding and bonding characteristics of the VB1 and VB2 states, which come from the hybridization between the electronic structures of these two sublayers. The bonding characteristics of the VB2 at Γ point shows clearly a large overlap of the wave functions from the top and bottom layers, confirming the strong interlayer interaction in layered borophene.

IV. MECHANICAL PROPERTIES

A. Ideal strength and critical strain of layered borophene

Starting with the optimized borophene structures, tensile strain is applied in either uniaxial (armchair or zigzag) or biaxial direction to explore the ideal tensile strength and the critical strain (the strain at which ideal strength reaches). With each uniaxial strain applied, the lattice constant along the transverse direction and boron atoms is fully relaxed. For biaxial strain, equibiaxial tension is applied and boron atoms in the unit cell are fully relaxed. We calculate the stress-strain relation of 2D layered borophene systems using the method described in the 2D black phosphorene [48]. In a 2D system,

the stress is expressed by multiplying the Cauchy stresses and Z/n to obtain the equivalent stress, where Z is the thickness of unit cell along the vacuum direction and n is the layer number of the system. To validate our calculations, we compute the mechanical properties of monolayer borophene, such as the elastic stiffness constants and Poisson's ratios shown in Table I, which are consistent with previous values [8,51].

Figures 5(a)–5(c) present our calculated stain-stress rela-tions. The stress-strain behaviors of layered borophene become nonlinear as the applied strain increases, similar to the case of monolayer structure [51]. From monolayer to layered borophene, the ideal strength along the armchair direction slightly increases from 24.0 N/m (monolayer) [51] to 25.2–26.3 N/m (few layer). This suggests that the outstanding large tensile strength of borophene is maintained in layered structure, which is crucial for the mechanical application of few-layer borophene. This maintenance can be explained by the change of the σ bond. The σ bond length in layered structure is 1.610 Å, which is shorter than that of monolayer (1.613 Å). On the other hand, the ideal strengths of layered borophene are 9.5–9.8 N/m along the zigzag direction, smaller than that of monolayer (12.4 N/m). The decrease originates from the enhancement of multicenter bonds by reducing the corresponding bond lengths from monolayer (1.855 Å) [51] to multilayer (1.836 Å). For the biaxial tension case, the curve has a maximum value of 21.0 N/m, larger than that of monolayer (19.2 N/m) [51]. The ideal strength of borophene is smaller than those of graphene (36.74–40.41 N/m), but larger than those of silicene (5.26–7.59 N/m), MoS_2 (9.59–14.75 N/m), and black phosphorene (4.44–9.99 N/m) [51]. Considering the tiny changes of lattice constants and ideal tensile strengths, we

TABLE I. The calculated elastic stiffness constants, Young's modulus, and Poisson's ratios for monolayer and layered borophene. The Poisson's ratios obtained from pure PBE without vdW corrections are given in parentheses for comparison. There are four nonzero elastic constants for 2D borophene because of their orthogonal primitive cell. The calculated values of monolayer structure are in good agreement with previous theoretical results.

System	Elastic stiffness constants (GPa nm)				Young's modulus (GPa nm)		Poisson's ratio	
	C_{11}	C_{22}	C_{66}	C_{12}	E_x	E_y	ν_{xy}	ν_{yx}
One-layer	396.6	158.4	86.5	−3.47	397	158	−0.022	−0.009
One-layer [46]	377.0	161.0	84.0	1.00	377	162	0.005	0.002
One-layer [46]	405.0	172.0	96.0	−1.00	405	172	−0.006	−0.003
One-layer [8]	398.0	170.0	94.0	−7.00	398	170	−0.040	−0.020
Two-layer	380.0	143.8	75.2	7.44	380	144	0.052(−0.063)	0.020(−0.031)
Three-layer	361.1	141.5	72.5	11.29	360	141	0.080(−0.039)	0.031(−0.018)
Four-layer	337.9	136.0	70.8	12.37	338	136	0.091(−0.104)	0.037(−0.050)

check the values by improving calculation accuracy and find that the aforementioned values are robust.

Unlike the increasing tensile strength along the armchair direction and decreasing strength along the zigzag direction from monolayered to layered borophene, the critical strain is always increasing in all engineered directions with the increasing number of layers, similar to the trend of black phosphorene [48]. For example, the critical strains are 14% (armchair), 15%–16% (zigzag), and 14%–16% (biaxial) for few-layer borophene, which are larger than those corresponding critical strains (10% armchair, 12% zigzag, 13% biaxial) in monolayer structure [51]. The increase of critical strains means that the mechanical flexibility of borophene is enhanced from monolayer to multilayer. We note that the increasing critical strains for few-layer borophene are still smaller than those of other 2D materials, such as graphene (19%–27%), black phosphorene (27%–33%), and MoS$_2$ (18%–26%) [51]. To summarize, few-layer borophene exhibit strong anisotropic responses for these three types of applied strains from the stress-strain curves.

B. Buckling height of layered borophene

Buckling height is a critical parameter for buckled 2D materials, obviously different from other flat 2D systems. We therefore investigate the dependencies of buckling height of layered borophene on three types of applied tension in Fig. 6. From monolayer to multilayer, the trends of buckling height dependent on tension are nearly the same, showing highly anisotropic and nonmonotonic. The buckling heights decrease sharply at the strain of 14% along the armchair direction, and 15%–16% along the biaxial direction, exactly corresponding to the critical strains of few-layer systems. The layered borophene turns into a graphenelike planar structure instead of the original buckling structure when the strain approaches 19% (16%–17%) along the armchair (biaxial) direction. Such turning means that the original borophene structure becomes unstable and is destroyed because of the phonon instability. On the contrary, if tension is applied along the zigzag direction, the buckling height increases monotonically with the increasing strain. It means that the out-of-plane Poisson's ratios are negative for layered borophene, similar to monolayer borophene [51]. This is because B1–B3 bonding along the zigzag direction decreases with increasing strain along this direction. The anisotropic out-of-plane Poisson's ratios in few-layer borophene are different from other flat 2D isotropic materials, for example, the layered graphene, h-BN, and MoS$_2$ have negative, near zero, and positive out-of-plane Poisson's ratios, respectively [60].

C. Mechanical constants of layered borophene

In addition to the stress-strain curves and buckling height dependence, we also calculate elastic constants, Young's modulus, and summarize them together with Poisson's ratios in Table I. Due to the anisotropy of the borophene structure,
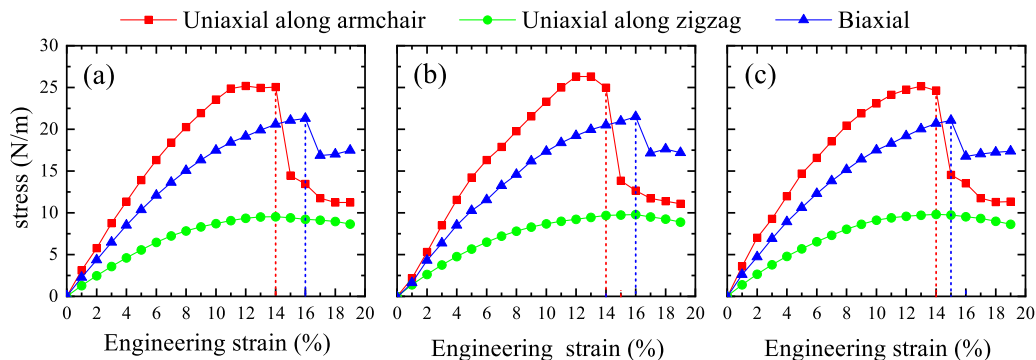
FIG. 5. The stress-strain relations for (a) bilayer, (b) trilayer, (c) four-layer borophene. The critical strains are 14% (along the armchair direction) and 15%–16% (along the biaxial direction).
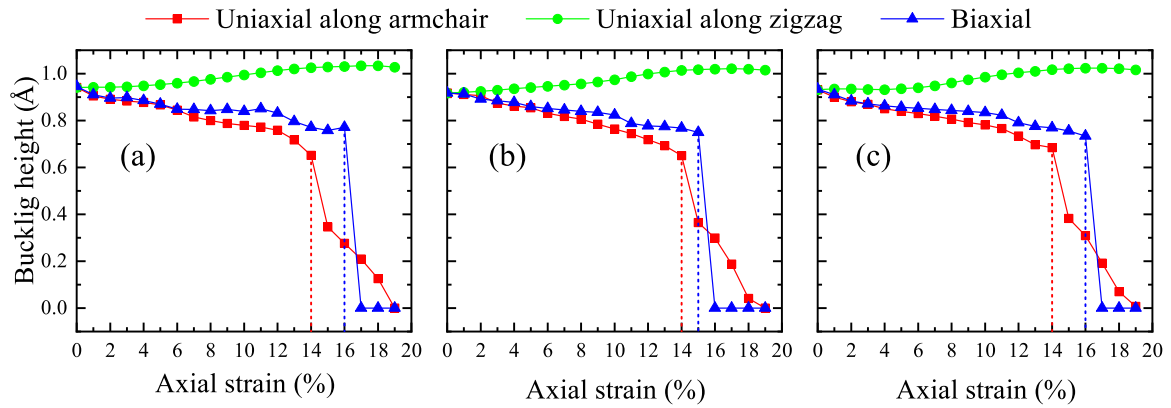
FIG. 6. The calculated dependence of buckling heights of (a) bilayer, (b) trilayer, (c) four-layer borophene under three types of tension. The buckling heights decrease sharply at the critical strain (14%) point, and drop to zero at the uniaxial along a of 20%.

the elastic constants, Young's modulus, and Poisson's ratios have different values along the zigzag and the armchair directions. From monolayer to few-layer borophene, the Young's modulus are decreasing from 396.6 GPa nm (armchair) and 158.4 GPa nm (zigzag) to 337.9 GPa nm (armchair) and 136.0 GPa nm (zigzag). This decreasing trend also appears in the buckled black phosphorus [48]. For both monolayer and few-layer borophene, the Young's modulus along the armchair direction is about 2.5 times larger than their counterparts along the zigzag direction, indicating that it is more difficult to apply strain along the armchair direction. One may notice that the Young's modulus of four-layer borophene along the armchair direction is still very large. This is because the interlayer interactions have negligible influence to the strong σ bond along the armchair direction. The large Young's modulus along the armchair direction suggests that few-layer borophene, similar to monolayer borophene, demonstrates superhardness compared to other 2D materials. This makes borophene a great candidate for practical large-magnitude-strain engineering.

Poisson's ratios measure the fundamental mechanical responses of solid against external loads. The out-of-plane Poisson's ratio, which is related to the change of the buckling height, has been discussed in a previous section. We will thus focus on the following in-plane Poisson's ratios in few-layer

borophene. For an applied strain ε along the armchair direction in the monolayer, the responding strain ε_V occurs along the zigzag direction as shown in Fig. 7(a). When a strain (ε) is applied along the armchair direction, the ε_V roughly increases with the increasing strain. That is, the larger the lattice constant a is, the larger the lattice constant b is. If a strain is applied along the zigzag direction, the ε_V tends to increase with the increasing strain in the range from -16% to 10%. This range is within the critical strains along the zigzag direction for monolayer borophene. Monolayer borophene therefore shows negative in-plane Poisson's ratio of -0.022 along x and -0.009 along y directions, confirming the anisotropic mechanical properties and in good agreement with previous results [8]. Considering large compression may include some ripples in primitive cell, we use 5×3 monolayer and bilayer supercells under compression strain of 20%, and find that there is no rippling. The large compression strain can also be found in graphene (up to 50%) [61].

For few-layer borophene, it is surprising to find that the negative in-plane Poisson's ratio in monolayer borophene dramatically changes into positive, for example, 0.052 along x and 0.020 along y directions in bilayer borophene, as shown in Table I. We should emphasize that this observation is totally different from other 2D materials, even for puckered black
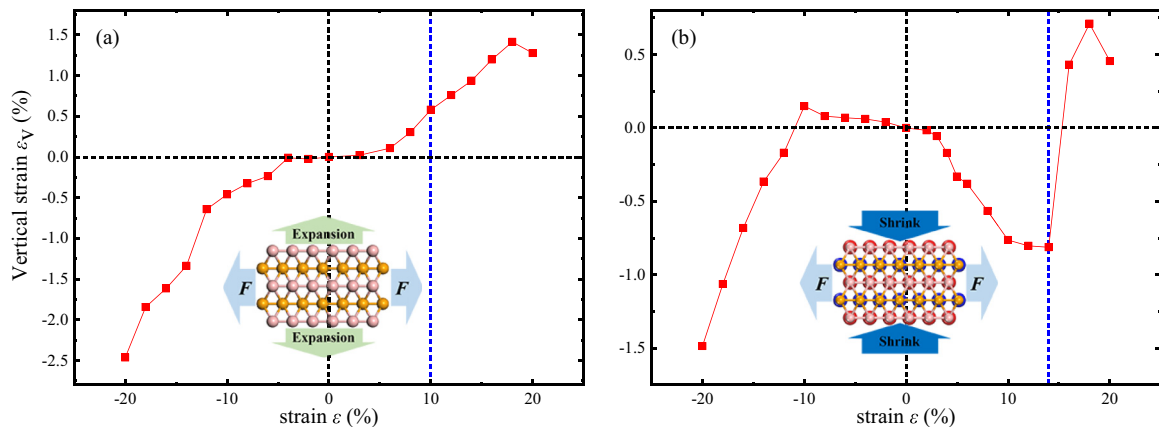
FIG. 7. The vertical strain ε_V versus applied strain ε along the armchair direction for monolayer (a) and bilayer (b) borophene, respectively. The positive (negative) ε means a tensile (compressive) strain. The blue dashed lines indicate positive critical strains of borophene. The negative critical strains are up to 50% based on a 5×3 supercell calculation. We thus do not mark the negative critical strain.
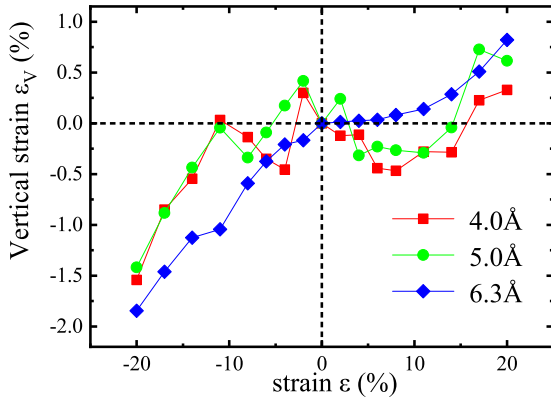
FIG. 8. The vertical strain ε_V versus applied strain ε along the armchair direction for varying interlayer distance 4.0 Å, 5.0 Å, 6.3 Å for bilayer borophene, respectively. The vdW interaction is in principle inverse proportion to the layer distance.

phosphorus and arsenene in which the negative Poisson's ratios are preserved from monolayer to multilayer [62,63]. In order to check the reliability of the positive Poisson's ratio in few-layer borophene, we show in Fig. 7(b) the responding strain ε_V for applied strain ε for bilayer borophene as an example, intuitively reflecting the Poisson's ratio. Very different from the case of monolayer borophene, the vertical strain ε_V is negative (positive) when the engineered strain is positive (negative) and smaller (larger) than 14% (−10%) in bilayer borophene, indicating a positive Poisson's ratio along the armchair direction. For the applied strain along the zigzag direction, the curve of ε_V versus ε is similar to the case of armchair direction, indicating also a positive Poisson's ratio. We note that the engineered strains considered here are within the range of the corresponding critical strains, and these results confirm the positive Poisson's ratios shown in Table I.

The dramatic change of the in-plane Poisson's ratio, i.e., from negative in the monolayer to positive in the multilayer, does not appear in other 2D materials. Without vdW corrections, the Poisson's ratios of layered borophene remain negative as shown in Table. I. This comparison confirms that the change of Poisson's ratios originates from the strong interlayer vdW interactions, as we discussed in previous sections [see the strong interlayer bonding states shown in Fig. 4(b)]. The interlayer interactions in 2D materials are in general much weaker comparing to the intralayer interactions, even in puckered atomic structures such as black phosphorus and arsenene. As a further check of the influence of the vdW interaction, we investigate the change of Poisson's ratio by varying the interlayer distance in few-layer borophene. Using bilayer borophene as an example, we analyze the curve of vertical strain ε_V for applied ε along the armchair direction, as displayed in Fig. 8. It is clear that with different interlayer distance, the curves of vertical strain ε_V versus ε become very different. When the interlayer distance approaches 6.3 Å, the curve becomes similar to that of monolayer borophene, with the negative Poisson's ratio recovered. This confirms that the vdW interlayer interactions are much stronger in metallic borophene than that in semiconducting 2D materials (such as flat TDMCs and puckered black phosphorus), resulting in a shorter interlayer distance and therefore intensively altering the

mechanical properties of few-layer borophene. Furthermore, as discussed in Refs. [60,64], the energy of the interlayer vdW interactions for 2D thick metals is proportional to d^{-2} (where d is the interlayer distance), while the asymptotic vdW energy of parallel structures is proportional to d^{-4} for 2D insulators. Thus, the decay speed of vdW interactions in few-layer metallic borophene is significantly slower than that in semiconducting black phosphorus and arsenene.

V. CONCLUSION

In conclusion, we have studied electronic and mechanical properties of few-layer borophene based on the buckled 2-*Pmmn* monolayer structure as synthesized by Mannix *et al.* in Ref. [8]. We find that the AA stacking mode is the most stable one among the six high-symmetry stacking configurations for bilayer structures. From monolayered to layered borophene, the robust anisotropic metallic features are maintained, with large energy splitting at Γ point (∼1.7 eV), confirming strong interlayer vdW interactions. Since the layered structures can withstand larger critical strains than that in monolayer, layered borophene exhibits more flexibility than monolayer one. Because of the preserved multicenter bonds along the zigzag direction, the out-of-plane negative Poisson's ratios are preserved. In contrast, the in-plane negative Poisson's ratios in the monolayer become positive in layered borophene. This novel phenomenon is a direct consequence of the very strong vdW interlayer interactions, and the negative Poisson's ratios could recover if the interlayer distance is increased to 6.3 Å artificially. The dramatic change of the in-plane Poisson's ratio from monolayer to multilayer does not appear in other 2D materials, even in puckered black phosphorus and arsenene. We hope that our theoretical results will inspire considerable experimental enthusiasm of few-layer borophene, especially for potential applications in novel electronic and mechanical devices.

APPENDIX

The geometric and electronic properties of 2D borophene change with the increasing layer, which are listed in Table II.

TABLE II. Optimized lattice constants (*a* and *b*), interlayer distances *d*, band gaps at Γ point (energy difference between highest occupied state and lowest unoccupied state), and band-splitting values at Γ point of monolayer, bilayer, trilayer, and four-layer borophene.

System	a (Å)	b (Å)	d (Å)	E_{gap} (eV)	E_{split} (eV)
One-layer	1.613	2.880		4.326	
Two-layer	1.610	2.898	3.072	3.263	1.681
Three-layer	1.611	2.894	2.957	2.219	1.358
Four-layer	1.609	2.894	2.956	2.117	1.039

[1] X. Sun, X. F. Liu, J. Yin, J. Yu, Y. Li, Y. Hang, X. C. Zhou, M. L. Yu, J. D. Li, G. A. Tai, and W. L. Guo, Adv. Funct. Mater. **27**, 1603300 (2017).

[2] T. Ogitsu, F. Gygi, J. Reed, Y. Motome, E. Schwegler, and G. Galli, J. Am. Chem. Soc. **131**, 1903 (2009).

[3] X. F. Zhou, X. Dong, A. R. Oganov, Q. Zhu, Y. J. Tian, and H. T. Wang, Phys. Rev. Lett. **112**, 085502 (2014).

[4] K. C. Lau and R. Pandey, J. Phys. Chem. C **111**, 2906 (2007).

[5] X. F. Zhou, A. R. Oganov, Z. H. Wang, I. A. Popov, A. I. Boldyrev, and H. T. Wang, Phys. Rev. B **93**, 085406 (2016).

[6] A. Lopez-Bezanilla and P. B. Littlewood, Phys. Rev. B **93**, 241405 (2016).

[7] X. J. Wu, J. Dai, Y. Zhao, Z. W. Zhuo, J. L. Yang, and X. C. Zeng, ACS Nano **6**, 7443 (2012).

[8] A. J. Mannix, X. F. Zhou, B. Kiraly, J. D. Wood, D. Alducin, B. D. Myers, X. L. Liu, B. L. Fisher, U. Santiago, J. R. Guest, M. J. Yacaman, A. Ponce, A. R. Oganov, M. C. Hersam, and N. P. Guisinger, Science **350**, 1513 (2015).

[9] B. Feng, J. Zhang, Q. Zhong, W. Li, S. Li, H. Li, P. Cheng, S. Meng, L. Chen, and K. Wu, Nat. Chem. **8**, 563 (2016).

[10] B. J. Feng, J. Zhang, R. Y. Liu, T. Iimori, C. Lian, H. Li, L. Chen, K. H. Wu, S. Meng, F. Komori, and I. Matsuda, Phys. Rev. B **94**, 041408 (2016).

[11] B. Feng, O. Sugino, R. Y. Liu, J. Zhang, R. Yukawa, M. Kawamura, T. Iimori, H. Kim, Y. Hasegawa, H. Li, L. Chen, K. Wu, H. Kumigashira, F. Komori, T. C. Chiang, S. Meng, and I. Matsuda, Phys. Rev. Lett. **118**, 096401 (2017).

[12] A. H. C. Neto, F. Guinea, N. M. R. Peres, K. S. Novoselov, and A. K. Geim, Rev. Mod. Phys. **81**, 109 (2009).

[13] A. Lherbier, A. R. Botello-Mendez, and J. C. Charlier, 2D Mater. **3**, 045006 (2016).

[14] J. C. Alvarez-Quiceno, R. H. Miwa, G. M. Dalpian, and A. Fazzio, 2D Mater. **4**, 025025 (2017).

[15] B. Peng, H. Zhang, H. Z. Shao, Y. F. Xu, R. J. Zhang, and H. Y. Zhua, J. Mater. Chem. C **4**, 3592 (2016).

[16] Q. H. Wang, K. Kalantar-Zadeh, A. Kis, J. N. Coleman, and M. S. Strano, Nat. Nanotechnol. **7**, 699 (2012).

[17] Y. F. Liang, S. T. Huang, R. Soklaski, and L. Yang, Appl. Phys. Lett. **103**, 042106 (2013).

[18] D. Y. Qiu, F. H. da Jornada, and S. G. Louie, Phys. Rev. Lett. **111**, 216805 (2013).

[19] A. Ramasubramaniam, Phys. Rev. B **86**, 115409 (2012).

[20] H. X. Zhong, S. Y. Gao, J. J. Shi, and L. Yang, Phys. Rev. B **92**, 115438 (2015).

[21] F. Xia, H. Wang, and Y. Jia, Nat. Commun. **5**, 4458 (2014).

[22] D. Malko, C. Neiss, F. Vines, and A. Gorling, Phys. Rev. Lett. **108**, 086804 (2012).

[23] T. Cheng, H. F. Lang, Z. Z. Li, Z. F. Liu, and Z. R. Liu, Phys. Chem. Chem. Phys. **19**, 23942 (2017).

[24] L. C. Xu, A. J. Du, and L. Z. Kou, Phys. Chem. Chem. Phys. **18**, 27284 (2016).

[25] E. S. Penev, A. Kutana, and B. I. Yakobson, Nano Lett. **16**, 2522 (2016).

[26] R. C. Xiao, D. F. Shao, W. J. Lu, H. Y. Lv, J. Y. Li, and Y. P. Sun, Appl. Phys. Lett. **109**, 122604 (2016).

[27] F. Scarpa, IEEE Signal Process. Mag. **25**, 128 (2008).

[28] Y. T. Sun and N. Pugno, Materials **6**, 699 (2013).

[29] Y. Prawoto, Comput. Mater. Sci. **58**, 140 (2012).

[30] K. E. Evans and A. Alderson, Adv. Mater. **12**, 617 (2000).

[31] K. F. Mak, C. Lee, J. Hone, J. Shan, and T. F. Heinz, Phys. Rev. Lett. **105**, 136805 (2010).

[32] Y. Zhang, T. R. Chang, B. Zhou, Y. T. Cui, H. Yan, Z. K. Liu, F. Schmitt, J. Lee, R. Moore, Y. L. Chen, H. Lin, H. T. Jeng, S. K. Mo, Z. Hussain, A. Bansil, and Z. X. Shen, Nat. Nanotechnol. **9**, 111 (2014).

[33] A. Splendiani, L. Sun, Y. Zhang, T. Li, J. Kim, C. Y. Chim, G. Galli, and F. Wang, Nano Lett. **10**, 1271 (2010).

[34] N. Karmodak and E. D. Jemmis, J. Phys. Chem. C **122**, 2268 (2018).

[35] P. E. Blochl, Phys. Rev. B **50**, 17953 (1994).

[36] G. Kresse and J. Furthmuller, Comput. Mater. Sci. **6**, 15 (1996).

[37] G. Kresse and D. Joubert, Phys. Rev. B **59**, 1758 (1999).

[38] J. Klimes, D. R. Bowler, and A. Michaelides, Phys. Rev. B **83**, 195131 (2011).

[39] M. Dion, H. Rydberg, E. Schroder, D. C. Langreth, and B. I. Lundqvist, Phys. Rev. Lett. **92**, 246401 (2004).

[40] J. P. Perdew, K. Burke, and M. Ernzerhof, Phys. Rev. Lett. **77**, 3865 (1996).

[41] H. J. Monkhorst and J. D. Pack, Phys. Rev. B **13**, 5188 (1976).

[42] J. D. Pack and H. J. Monkhorst, Phys. Rev. B **16**, 1748 (1977).

[43] S. Maintz, V. L. Deringer, A. L. Tchougreeff, and R. Dronskowski, J. Comput. Chem. **37**, 1030 (2016).

[44] J. Zhou and R. Huang, J. Phys. Chem. Solids **56**, 1609 (2008).

[45] S. H. Zhang, J. Zhou, Q. Wang, X. S. Chen, Y. Kawazoe, and P. Jena, Proc. Natl. Acad. Sci. USA **112**, 2372 (2015).

[46] V. Wang and W.-T. Geng, J. Phys. Chem. C **121**, 10224 (2017).

[47] V. Wang, Vaspkit, a post-processing program for the VASP code, 2013.

[48] Q. Wei and X. Peng, Appl. Phys. Lett. **104**, 251915 (2014).

[49] A. Togo, F. Oba, and I. Tanaka, Phys. Rev. B **78**, 134106 (2008).

[50] S. Nosé, J. Chem. Phys. **81**, 511 (1984).

[51] H. F. Wang, Q. F. Li, Y. Gao, F. Miao, X. F. Zhou, and X. G. Wan, New J. Phys. **18**, 073016 (2016).

[52] H. Braunschweig and R. D. Dewhurst, Angew. Chem. Int. Ed. **52**, 3574 (2013).

[53] N. Gao, X. Wu, X. Jiang, Y. Bai, and J. Zhao, FlatChem **7**, 48 (2018).

[54] T. Ohta, A. Bostwick, T. Seyller, K. Horn, and E. Rotenberg, Science **313**, 951 (2006).

[55] J. E. Padilha and R. B. Pontes, J. Phys. Chem. C **119**, 3818 (2015).

[56] J. Dai and X. C. Zeng, J. Phys. Chem. Lett. **5**, 1289 (2014).

[57] A. Ramasubramaniam, D. Naveh, and E. Towe, Phys. Rev. B **84**, 205325 (2011).

[58] H. Zhong, R. Quhe, Y. Wang, Z. Ni, M. Ye, Z. Song, Y. Pan, J. Yang, L. Yang, M. Lei *et al.*, Sci. Rep. **6**, 21786 (2016).

[59] D. Rigby and R.-J. Roe, J. Chem. Phys. **89**, 5280 (1988).

[60] S. Woo, H. C. Park, and Y.-W. Son, Phys. Rev. B **93**, 075420 (2016).

[61] G. Tsoukleri, J. Parthenios, K. Papagelis, R. Jalil, A. C. Ferrari, A. K. Geim, K. S. Novoselov, and C. Galiotis, Small **5**, 2397 (2009).

[62] H. Wang, X. Li, P. Li, and J. Yang, Nanoscale **9**, 850 (2017).

[63] J. W. Han, J. F. Xie, Z. Y. Zhang, D. Z. Yang, M. S. Si, and D. S. Xue, Appl. Phys. Express **8**, 041801 (2015).

[64] J. F. Dobson, A. White, and A. Rubio, Phys. Rev. Lett. **96**, 073201 (2006).